


Experimental Characterization of Acoustic Streaming in Gradients of Density and Compressibility

Wei Qiu,^{1,*} Jonas T. Karlsen,^{1,†} Henrik Bruus,^{1,‡} and Per Augustsson^{2,§}

¹*Department of Physics, Technical University of Denmark, DTU Physics Building 309, DK-2800 Kongens Lyngby, Denmark*

²*Department of Biomedical Engineering, Lund University, Ole Römers väg 3, 22363 Lund, Sweden*

 (Received 17 October 2018; revised manuscript received 21 December 2018; published 7 February 2019)

Suppression of boundary-driven Rayleigh streaming has recently been demonstrated for fluids of spatial inhomogeneity in density and compressibility owing to the competition between the boundary-layer-induced streaming stress and the inhomogeneity-induced acoustic body force. To understand the implications of this for acoustofluidic particle handling in the submicrometer regime, we here characterize acoustic streaming by general defocusing particle tracking inside a half-wavelength acoustic resonator filled with two miscible aqueous solutions of different density and speed of sound by adjusting the mass fraction of solute molecules. We follow the temporal evolution of the system as the solute molecules become homogenized by diffusion and advection. The acoustic streaming is suppressed in the bulk of the microchannel for 70–200 s, depending on the choice of inhomogeneous solutions. From confocal measurements of the concentration field of fluorescently labeled Ficoll solute molecules, we conclude that the temporal evolution of the acoustic streaming depends on the diffusivity and the initial distribution of these molecules. Suppression and deformation of the streaming rolls are observed for inhomogeneities in the solute mass fraction down to 0.1%.

DOI: [10.1103/PhysRevApplied.11.024018](https://doi.org/10.1103/PhysRevApplied.11.024018)

I. INTRODUCTION

Microfluidics has emerged as a tool to analyze biological particles by their biomechanical properties [1–4] and offers high-precision in-line sample processing for fast and automated isolation of rare cell populations, such as white blood cell (WBC) subpopulations [5,6]; circulating tumor cells [7–9]; and controlled high-throughput size fractionation of bionanoparticles, such as pathogens [10] and extracellular vesicles [11,12]. In recent studies, acoustofluidics has been highlighted as a label-free method for separation [13,14] and trapping [15] of submicrometer biological particles.

Acoustic manipulation of particles in the submicrometer range is challenging due to the presence of acoustic streaming associated with the acoustic field. Acoustic streaming is a steady flow that arises in a fluid medium interacting with sound waves. It has been studied extensively [16–20] because of its important role in thermoacoustics [21,22], medical ultrasound [23–26], and acoustic levitation [27,28]. Acoustic streaming has been classified

into two categories based on its formation mechanisms. One mechanism is the spatial attenuation of acoustic waves in the bulk of the fluid, which results in a time-averaged net force in the direction of the wave propagation [16,29]. This type of streaming, called quartz wind or bulk-driven Eckart streaming, is generally observed in large systems where the length scale of wave propagation is much longer than the wavelength. The other mechanism, predominant in systems of a size comparable to the wavelength, such as the system under investigation in this work, is that of acoustic energy dissipation in the viscous boundary layers, where the velocity of the oscillating fluid decays to match the velocity of the boundary [30,31] of either walls [17,32,33] or suspended objects [28,34–36]. This boundary-driven so-called Rayleigh streaming typically generates a recirculating flow in the bulk.

Rayleigh streaming has been identified as a key limiting factor in standing-wave, acoustic particle manipulation [37–43] because suspended microparticles are subject to both acoustic radiation forces and Stokes drag forces from the acoustic streaming. The relative magnitude of the two forces depends on the microparticle size and the material properties of the particle and the suspending fluid. For microparticles below a critical size, the motion of microparticles is dominated by acoustic streaming, which in many cases hinders the manipulation

*weiqiu@fysik.dtu.dk

†jonastkarlsen@gmail.com

‡bruus@fysik.dtu.dk

§per.augustsson@bme.lth.se

of submicrometer-sized particles. Manipulation below the classical limit has previously been demonstrated by flow vortices generated by two-dimensional acoustic fields [44, 45], by acoustically active seed particles [39], by a thin reflector design [46], or in systems actuated by surface acoustic waves [47–49].

Recently, we discovered that an acoustic body force can cause relocation and stabilization of inhomogeneities in fluids of spatially inhomogeneous density and compressibility when subjected to a standing-wave field [50–52]. This spurred the development of isoacoustic focusing, an equilibrium method to measure cell acoustic properties wherein cells migrate in a fluid of gradually increasing acoustic impedance to their points of zero acoustic contrast [1]. Furthermore, the acoustic body force caused by a spatial inhomogeneity in density was found to enable efficient suppression of acoustic streaming in the bulk inside a half-wavelength resonator [53]. This finding paves the way for acoustic manipulation, fractionation, and in-line sample preparation of submicrometer particles of biological relevance such as bacteria, viruses, and exosomes, as well as trapping of hot plasma in gasses [54].

Here, we extend the study of acoustic streaming to fluids made inhomogeneous in both the density and the speed of sound by the addition of different solute molecules, and we investigate its evolution in an ultrasound half-wavelength glass-silicon resonator with a rectangular cross section. The suppression of acoustic streaming is mapped for different combinations of gradients in the density and the speed of sound. The evolution of the acoustic streaming and the molecular concentration field is measured in fluids of different solute molecule concentration and diffusivity by particle-tracking velocimetry and confocal microscopy, respectively. We conclude that the acoustic streaming is strongly dependent on inhomogeneities in the solute mass fraction down to 0.1%.

II. THEORY OF INHOMOGENEOUS ACOUSTOFLUIDICS

In our previous work [51–53], we have presented a continuum theory of the acoustic body force (or force density) \mathbf{f}_{ac} as well as of the acoustic streaming and its suppression in an inhomogeneous fluid. In the following, we briefly summarize this theory, but refer the reader to the original papers [51–53] for a full account of the theory. We consider a fluid that is made inhomogeneous by adding solute molecules with dilute-limit diffusivity D and a spatiotemporal-dependent mass fraction (concentration) $s = s(\mathbf{r}, \tau)$. The physical properties of the resulting solution thus depend on space and time through s : density $\rho_0(s)$, sound speed $c_0(s)$, compressibility $\kappa_0(s) = (\rho_0 c_0^2)^{-1}$, dynamic viscosity $\eta_0(s)$, and bulk viscosity η_0^b . Moreover, the solute molecules have an s -dependent diffusivity $D(s)$. As discussed in Refs. [51–53], a crucial

property of this system, when placed in an ultrasound field, is the separation of time scales between the fast acoustics $t \sim 0.1 \mu\text{s}$ and the slow hydrodynamics $\tau \sim 10 \text{ ms}$. Because $\tau \sim 10^5 t$, the acoustic fields can be computed while keeping the hydrodynamic degrees of freedom fixed at each instance in time τ .

A. Fast-time-scale acoustics

The inhomogeneous solution is placed in an acoustic cavity where a time-harmonic standing acoustic wave is imposed at frequency f and angular frequency $\omega = 2\pi f$. We assume the usual adiabatic case for the first-order pressure field p_1 ; density field ρ_1 ; and velocity field \mathbf{v}_1 of amplitude p_{ac} , ρ_{ac} , and v_{ac} , respectively. The stress is $\boldsymbol{\sigma}_1 = -p_1 \mathbf{I} + \eta_0 [\nabla \mathbf{v}_1 + (\nabla \mathbf{v}_1)^T] + (\eta_0^b - \frac{2}{3} \eta_0) (\nabla \cdot \mathbf{v}_1) \mathbf{I}$, where the superscript T indicates tensor transposition. Writing each acoustic field in the form $\rho = \rho_0(\mathbf{r}, \tau) + \rho_1(\mathbf{r}, \tau) e^{-i\omega t}$, the governing equations become [53]

$$-i\omega \rho_0 \mathbf{v}_1 = \nabla \cdot \boldsymbol{\sigma}_1, \quad (1a)$$

$$-i\omega \kappa_0 p_1 = -\nabla \cdot \mathbf{v}_1, \quad (1b)$$

$$-i\omega \rho_0 \kappa_0 p_1 = -i\omega \rho_1 + \mathbf{v}_1 \cdot \nabla \rho_0. \quad (1c)$$

B. The acoustic body force

As we have shown in Ref. [51], the acoustic fields acting on the short time scale t give rise to an acoustic body force \mathbf{f}_{ac} acting on the inhomogeneous fluid on the slow time scale τ . This body force is derived from the nonzero divergence in the time-averaged (over one oscillation period $2\pi/\omega$) acoustic momentum-flux-density tensor $\langle \boldsymbol{\Pi} \rangle$,

$$\mathbf{f}_{\text{ac}} = -\nabla \cdot \langle \boldsymbol{\Pi} \rangle. \quad (2)$$

The second-order quantity $\langle \boldsymbol{\Pi} \rangle$ is given by products of the first-order acoustic fields p_1 and \mathbf{v}_1 [55],

$$\langle \boldsymbol{\Pi} \rangle = \langle p_2 \rangle \mathbf{I} + \langle \rho_0 \mathbf{v}_1 \mathbf{v}_1 \rangle, \quad (3)$$

where the second-order mean Eulerian excess pressure $\langle p_2 \rangle$ takes the form

$$\langle p_2 \rangle = \frac{1}{4} \kappa_0 |p_1|^2 - \frac{1}{4} \rho_0 |\mathbf{v}_1|^2. \quad (4)$$

The acoustic body force \mathbf{f}_{ac} was derived on the slow hydrodynamic time scale τ in Ref. [51] from the divergence of the time-averaged acoustic momentum-flux-density tensor induced by continuous spatial variations in the fluid density ρ_0 and compressibility κ_0 or equivalently in density ρ_0 and sound speed c_0 :

$$\mathbf{f}_{\text{ac}} = -\frac{1}{4} |p_1|^2 \nabla \kappa_0 - \frac{1}{4} |\mathbf{v}_1|^2 \nabla \rho_0 \quad (5a)$$

$$= \frac{1}{4} (\kappa_0 |p_1|^2 - \rho_0 |\mathbf{v}_1|^2) \frac{\nabla \rho_0}{\rho_0} + \frac{1}{2} \kappa_0 |p_1|^2 \frac{\nabla c_0}{c_0}. \quad (5b)$$

C. Slow-time-scale dynamics

The dynamics on the slow time scale τ is governed by the momentum- and mass-continuity equations for the fluid velocity $\mathbf{v}(\mathbf{r}, \tau)$ and pressure $p(\mathbf{r}, \tau)$ and by the advection-diffusion equation for the mass fraction (concentration) $s(\mathbf{r}, \tau)$ of the solute with diffusivity D [51]:

$$\partial_\tau(\rho_0 \mathbf{v}) = \nabla \cdot [\boldsymbol{\sigma} - \rho_0 \mathbf{v} \mathbf{v}] + \mathbf{f}_{\text{ac}} + \rho_0 \mathbf{g}, \quad (6a)$$

$$\partial_\tau \rho_0 = -\nabla \cdot (\rho_0 \mathbf{v}), \quad (6b)$$

$$\partial_\tau s = -\nabla \cdot [-D \nabla s + \mathbf{v} s]. \quad (6c)$$

Here, \mathbf{g} is the gravitational acceleration, $\boldsymbol{\sigma}$ is the fluid stress tensor, and \mathbf{f}_{ac} is the acoustic body force.

D. Boundary-driven acoustic streaming

The above slow-time-scale velocity field \mathbf{v} comprises the acoustic streaming in the general inhomogeneous case, which is the main focus of this work. However, as the inhomogeneity in our system is smeared out by diffusion as time passes, it is helpful to be reminded of the streaming flow in homogeneous systems. This problem was solved analytically by Lord Rayleigh [30] for an infinite parallel-plate channel of height H with its two plates placed symmetrically around the x - y plane at $z = \pm \frac{1}{2}H$ and with the imposed first-order standing-wave acoustic fields with wavelength λ and wave number $k = (2\pi/\lambda)$ along the y direction \mathbf{e}_y : $p_1(y) = p_{\text{ac}} \sin(ky) e^{-i\omega t}$ and $\mathbf{v}_1 = v_{\text{ac}} \cos(ky) e^{-i\omega t} \mathbf{e}_y$. In the case of $\lambda \gg H \gg \delta$, where $\delta = \sqrt{2\eta_0/(\rho_0 \omega)}$ is the thickness of the viscous boundary layer, Rayleigh found the time-averaged components $\langle v_{2y} \rangle$ and $\langle v_{2z} \rangle$ of the second-order fluid velocity $\langle \mathbf{v}_2(y, z) \rangle$ outside the viscous boundary layer to be

$$\langle v_{2y} \rangle = \frac{3}{8} \frac{v_{\text{ac}}^2}{c_0} \sin(2ky) \left[1 - 3 \frac{(2z)^2}{H^2} \right] \frac{1}{2}, \quad (7a)$$

$$\langle v_{2z} \rangle = \frac{3}{8} \frac{v_{\text{ac}}^2}{c_0} \cos(2ky) \left[\frac{2z}{H} - \frac{(2z)^3}{H^3} \right] \frac{kH}{2}. \quad (7b)$$

For an analytical solution in a closed rectangular channel, see Ref. [33]. In any case, the amplitudes p_{ac} and v_{ac} are related to each other and the acoustic energy density E_{ac} :

$$E_{\text{ac}} = \frac{1}{4} \rho_0 v_{\text{ac}}^2 = \frac{1}{4} \kappa_0 p_{\text{ac}}^2. \quad (8)$$

E. Numerical simulations of the system

In our previous work [51–53], we have presented how to carry out numerical simulations of acoustofluidics in an inhomogeneous fluid. In the following, we briefly summarize this method, but refer the reader to the original papers [51–53] for a full account and to Ref. [20] for a specific script simulating transient acoustofluidics. The

dynamics in the 2D channel cross section is solved numerically, under stop-flow conditions with the initial conditions described in Secs. IV B, using a weak-form finite-element implementation in COMSOL Multiphysics [56] with regular rectangular mesh elements. A segregated solver solves the time-dependent problem in two steps. (i) The fast-timescale acoustics Eq. (1) in the inhomogeneous medium is solved while keeping the hydrodynamic degrees of freedom fixed. This process allows computation of the time-averaged acoustic body force \mathbf{f}_{ac} , Eq. (5). (ii) The slow-timescale dynamics Eq. (6) is then integrated in time τ while keeping the acoustic energy density fixed at $E_{\text{ac}} = 52$ Pa [57]. This implementation extends our previous one limited to iodixanol solutions [53] by allowing for $\nabla c_0 \neq 0$ and an s -dependent diffusivity $D(s)$.

III. MATERIALS AND METHODS

A. Experimental setup and materials

The silicon chip consists of a straight channel of length $L = 24$ mm, width $W = 375 \mu\text{m}$, and height $H = 133 \mu\text{m}$, as sketched in Fig. 1. The chip is sealed by a Pyrex lid of thickness 1 mm using anodical bonding and an $18 \times$

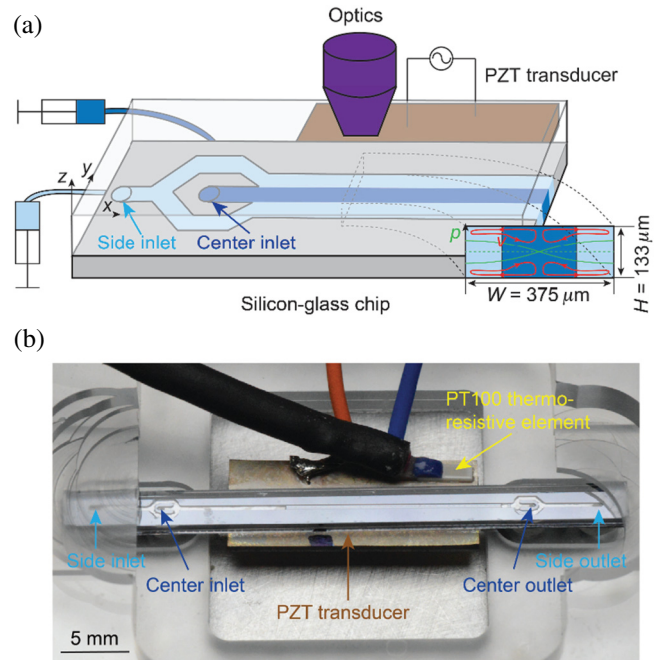


FIG. 1. (a) Sketch of the acoustofluidic silicon chip (gray) sealed with a glass lid, which allows optical recording (purple) of the tracer bead motion (red trajectories) in the channel cross section of width $W = 375 \mu\text{m}$ and height $H = 133 \mu\text{m}$. A Ficoll solution (dark blue) is injected into the center and laminated by pure water (light blue). The piezoelectric transducer (brown) excites the resonant half-wave pressure field p_1 (inset, green) at 2 MHz. (b) Top-view photograph of the chip (dark gray) mounted on the PZT transducer (brown) and placed in its holder (transparent plastic).

6.4 × 1.0-mm lead zirconate titanate (PZT) transducer (PZT26, Ferroperm Piezoceramics, Denmark) is bonded underneath using cyanoacrylate glue (Loctite Super Glue, Henkel Norden AB, Stockholm, Sweden). At the main channel inlet, three streams join in a trifurcation of which the two side streams are routed via a common port, while the center stream has a separate port. At the end of the main channel, the outlet has the same trifurcated configuration as the inlet. Pieces of silicone tubing (outer diameter 3 mm, inner diameter 1 mm, and length 7 mm) are glued to the chip inlets and outlets. The inlet flow streams are routed via a motorized four-port, two-way diagonal valve so that the flow can be stopped by a short circuit of the side inlets with the center inlet stream, and the outlet streams are routed via a two-port valve. The inlets are used for injecting two different liquids, whereas only one outlet is used for collecting the waste, while the other outlet is blocked during all measurements. A Pt100 thermoresistive element is bonded to the PZT transducer to record the temperature.

The PZT transducer is driven by a function generator (AFG3022B, Tektronix, Inc., Beaverton, Oregon, USA) and the waveforms of the applied voltages to the transducer are monitored by an oscilloscope (TDS1002, Tektronix, Inc., Beaverton, Oregon, USA). The liquids are injected into the channel using syringe pumps (neMESYS, Cetoni GmbH, Korbussen, Germany) with flow rates controlled by a computer interface.

The main density and speed-of-sound modifiers used for this study are Ficoll polymers (PM70 and PM400, GE Healthcare Biosciences AB, Uppsala, Sweden) of different average molecular masses (70,000 mol wt for PM70 and 400,000 mol wt for PM400). The Ficoll is dissolved in Milli-Q water to different mass fractions. The density and speed of sound of all the solutions are measured using a density and sound velocity meter (DSA 5000 M, Anton Paar GmbH, Graz, Austria) and the viscosities are measured by a falling-ball microviscometer (MINIVIS II, AMETEK Grabner Instruments, Vienna, Austria). We use the nine different solution combinations listed in Table I to create inhomogeneous acoustofluidics.

The measured material parameters of the Ficoll PM70 and Ficoll PM400 solutions used in the experiments at temperature $T = 25\text{ °C}$ are given in the Supplemental Material [58]. The resulting fitting expressions for these parameters are listed in Table II.

B. The GDPT setup and method

The acoustic streaming is studied by recording the motion of suspended tracer particles using the so-called general defocusing particle-tracking (GDPT) technique [59,60]. GDPT is a single-camera particle-tracking method, in which astigmatic images are employed by using a cylindrical lens. A unique defocused elliptical shape of a spherical tracer particle in the depth coordinate z can be

TABLE I. Specification of the nine inhomogeneous solutions S1–S9 used in the experiments. The excess density $\hat{\rho}_*$ and speed of sound \hat{c}_* are defined in Eq. (9). PBS is phosphate-buffered saline.

ID	Center inlet	Side inlet	$\hat{\rho}_*$ (%)	\hat{c}_* (%)
S1	5% Ficoll PM400	PBS	0.96	0.00
S2	10% Ficoll PM70	6.38% iodixanol	0.00	1.92
S3	15% iodixanol	10% Ficoll PM70	4.74	-2.13
S4	10% Ficoll PM400	Milli-Q water	3.51	1.69
S5	5% Ficoll PM400	Milli-Q water	1.72	0.77
S6	1% Ficoll PM400	Milli-Q water	0.34	0.19
S7	10% Ficoll PM70	Milli-Q water	3.51	1.69
S8	5% Ficoll PM70	Milli-Q water	1.71	0.79
S9	1% Ficoll PM70	Milli-Q water	0.34	0.17

provided in such a system, which enables robust three-dimensional tracking of particle motion in microfluidic systems.

The GDPT tracer particles in the solutions are suspensions of fluorescent green polystyrene beads with a nominal diameter of 0.49 μm (Molecular Probes, Thermo Fisher Scientific, Waltham, MA, USA). The images for the GDPT analysis of the tracer particle motion in the microchip are recorded using a CMOS camera (ORCA-Flash4.0 V3, Hamamatsu Photonics K.K., Japan) mounted on an epifluorescence microscope (BX51WI, Olympus Corporation, Tokyo, Japan). An objective lens with 10× magnification and 0.3 numerical aperture is used and a cylindrical lens with a focal length of 300 mm is placed between the camera and the objective at a distance of 20 mm in front of the camera. This configuration provides a measurement volume of $1.31 \times 1.52 \times 0.15\text{ mm}^3$. Blue light fluorescent excitation light is provided by a double-wavelength light-emitting-diode (LED) unit (pE-200^{ultra}, CoolLED Ltd., UK) with a peak wavelength of 488 nm. A standard fluorescence filter cube is used with an excitation

TABLE II. The measured density $\rho_0(s)$, sound speed $c_0(s)$, and viscosity $\eta_0(s)$, obtained as described in Sec. III A, as well as diffusivity $D(s)$ (see Sec. IV A), for homogeneous Ficoll–Milli-Q solutions as a function of the solute mass fraction (concentration) s in the interval $0 < s < 0.1$. The fits are based on 9 (for D only 3) values of s in that interval.

Ficoll PM70	
$\rho_0(s)$	$(1 + 0.349 s) 996.85\text{ kg m}^{-3}$
$c_0(s)$	$(1 + 0.167 s) 1496.30\text{ m s}^{-1}$
$\eta_0(s)$	$\exp(10.82 s) 0.893\text{ mPa s}$
$D(s)$	$(1 - 5.51 s + 23.0 s^2) 1.21 \times 10^{-10}\text{ m}^2\text{ s}^{-1}$
Ficoll PM400	
$\rho_0(s)$	$(1 + 0.348 s) 996.91\text{ kg m}^{-3}$
$c_0(s)$	$(1 + 0.164 s) 1496.50\text{ m s}^{-1}$
$\eta_0(s)$	$\exp(16.20 s) 0.893\text{ mPa s}$
$D(s)$	$(1 - 10.3 s + 56.0 s^2) 1.15 \times 10^{-10}\text{ m}^2\text{ s}^{-1}$

passband from 460 to 490 nm and a high-pass emission filter at 520 nm.

Before performing a GPDT measurement, a stack of calibration images is obtained with an interval of $1\ \mu\text{m}$ in the depth coordinate by moving a motorized z stage (MFD, Märzhäuser, Wetzlar GmbH & Co. KG, Wetzlar, Germany) equipped on the microscope. Then, the height of the stage is fixed and the motion of the particles is recorded. The image acquisition is performed with an exposure time of 90 ms and a frame rate of 10 frames/s. The acquired images are analyzed in GDPTlab by performing a normalized cross-correlation and comparing the acquired images with the calibration stack. Because the channel is filled with liquid, the values of liquid refractive indices are required for calculating the true particle positions in z coordinates, which are measured using an automatic refractometer (Abbemat MW, Anton Paar GmbH, Graz, Austria). The mean value of the refractive indices of the two liquids injected into the channel is used for particle tracking, which gives a maximum error of $1\ \mu\text{m}$ in the z direction. Finally, the particle trajectories and velocities are constructed. Particles are rejected if their cross-correlation peak amplitude is less than 0.95 and trajectories are rejected if they have less than six particle positions.

C. Experimental procedures

A laminated flow of two liquids is injected into the channel to form a concentration gradient with a flow rate of $100\ \mu\text{l}/\text{min}$ and a volumetric ratio near unity; see Fig. 1. Before and during the measurements, the transducer is actuated by a linear frequency sweep from 1.95 to 2.05 MHz in cycles of 1 ms to produce a standing half-wave across the width [61]. The frequency sweep covers the identified resonance frequencies at 1.96 MHz for pure water and 1.97 MHz for 10% Ficoll PM400 and ensures steady actuation throughout the experiment during the time evolution of the concentration field. The applied voltages (ranging from 1.59 to 1.67 V peak to peak) are adjusted for each injection of fluids to maintain the same acoustic energy density $E_{\text{ac}} \approx 52\ \text{Pa}$ in the channel. For the inhomogeneous situation with three liquid layers, we estimate $E_{\text{ac}} = \frac{1}{2}(E_{\text{ac}}^{\text{ctr}} + E_{\text{ac}}^{\text{side}})$, where $E_{\text{ac}}^{\text{ctr}}$ and $E_{\text{ac}}^{\text{side}}$ in the center and side layers are measured in their respective homogeneous states by tracking individual polystyrene beads with a nominal diameter of $6.33\ \mu\text{m}$ (PFP-6052, Kisker Biotech GmbH & Co. KG, Steinfurt, Germany) [62]. At time $\tau = 0$, the flow is stopped and the images for the GPDT measurements are recorded. The instantaneous stop of the flow in the channel is performed by short circuit of the two inlets by switching the four-port valve, which stops the flows and equilibrates the pressures of the two inlet streams; see Fig. 2. For each set of measurements, the particle motion is recorded for 200 s to observe the evolution

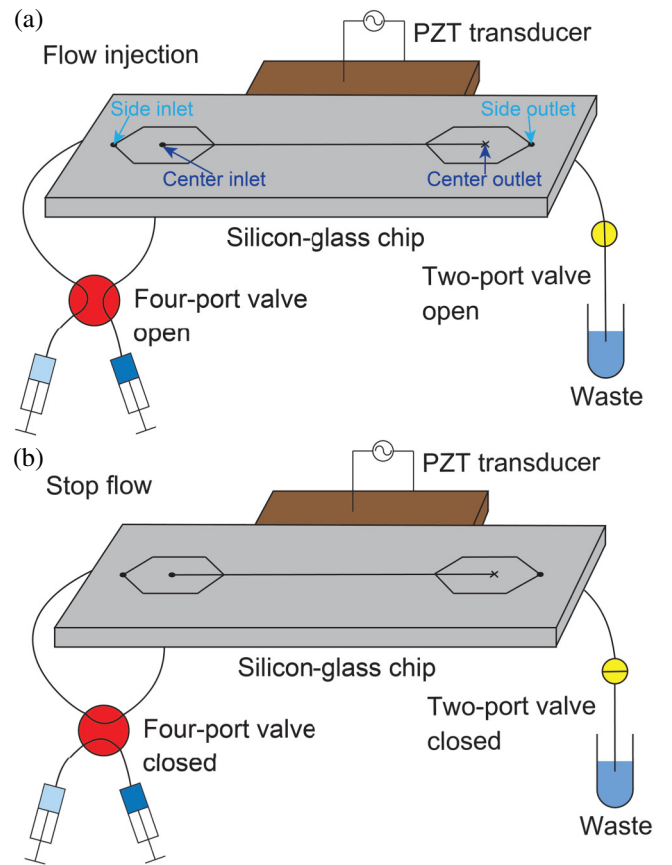


FIG. 2. Sketch of the stop-flow mechanism. (a) When the two liquids are injected, the two syringes are connected to the two inlets through the open four-port valve and the waste is collected through the open two-port valve. (b) To stop the flow, the two inlets are short circuited by closing the four-port valve and the outlet is blocked by closing the two-port valve. The center outlet is always blocked during the experiment.

of the acoustic streaming. Each measurement is repeated at least 16 times to improve the statistics.

The evolution of the concentration gradient in the channel is mapped by confocal microscopy (Fluoview 300, Olympus Corporation, Tokyo, Japan) in the x - y plane at the midheight of the channel ($z = 0$). The same objective lens as in the streaming measurement is used and a scan rate of $0.89\ \text{s}^{-1}$ is chosen, which provides a measurement area of $658 \times 385\ \mu\text{m}^2$. To trace the Ficoll concentration fields, fluorescein isothiocyanate- (FITC) labeled Ficoll (Polysucrose 70- and Polysucrose 400-fluorescein isothiocyanate conjugate, Sigma-Aldrich Sweden AB, Stockholm, Sweden) are added to the solutions in amounts ranging from 0.10% to 0.16%. Before the measurement of the concentration gradient, a background image is recorded when no fluorescent molecules are present in the channel. A linear decay of the intensity of the fluorescence signal emitted from FITC-labeled Ficoll solutions with the decreasing concentration is confirmed. After exciting the

sound field, the two liquids are laminated in the channel by infusing them with a total flow rate of $100 \mu\text{l}/\text{min}$ and, therefore, it takes them ~ 1 s to reach the observation region, which is 10 mm downstream from the trifurcation inlet. The acoustic energy density, the flow rate, and the volumetric ratio are the same as those in the streaming measurements. The image acquisition starts at $\tau = 5$ s after stopping the flow and continues until $\tau = 195$ s in intervals of 10 s. Each measurement is repeated three times.

IV. RESULTS AND DISCUSSION

A. Time evolution of concentration fields

The acoustofluidics of the inhomogeneous system is governed by the time evolution of the molecular concentration field s . By adding fluorescently tagged Ficoll molecules to the center flow stream, we study this evolution by confocal microscopy. For a given solution combination injected, confocal x - y scans are recorded at midheight ($z = 0$). In Fig. 3 is shown examples of such scans for solution S4 (10% PM400 and Milli-Q) of Table I

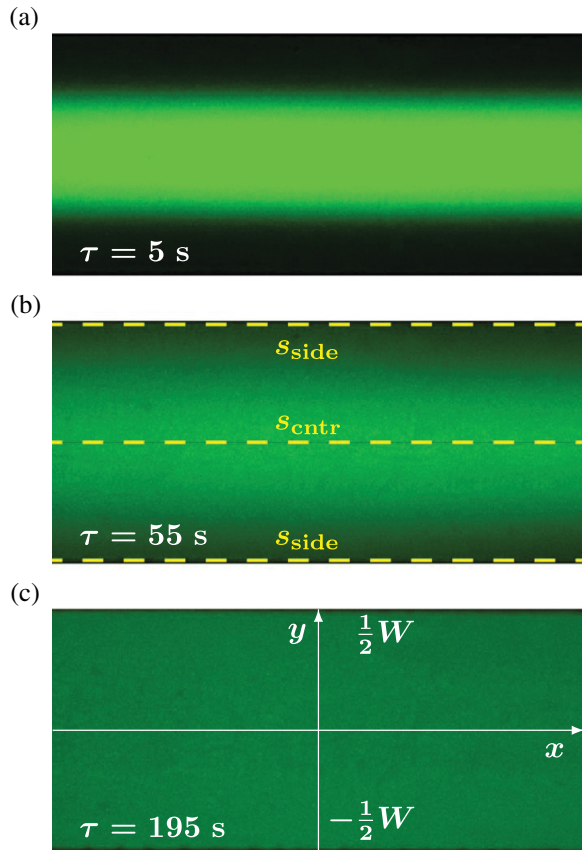


FIG. 3. Confocal images in the horizontal x - y plane taken of solution S4 with acoustics on at (a) $\tau = 5$ s, (b) $\tau = 55$ s, and (c) $\tau = 195$ s. The yellow lines indicate the locations where s_{cntr} and s_{side} are measured, which are then used to determine $\hat{\rho}_*$, \hat{c}_* , and \hat{s}_* ; see Eqs. (9) and (10).

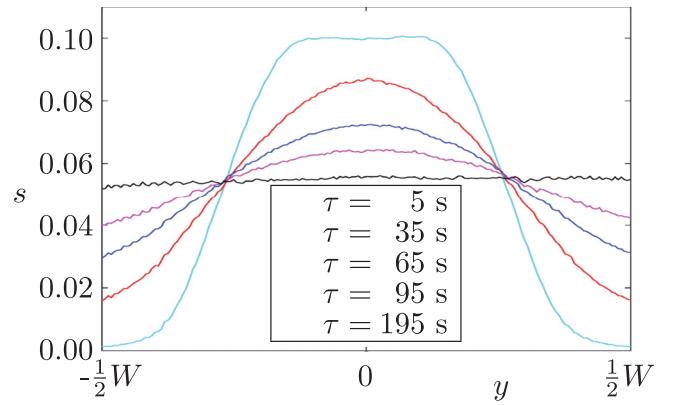


FIG. 4. The time evolution with acoustics present of the concentration profile for solution S4 with FITC-labeled Ficoll molecules deduced from recordings as shown in Fig. 3.

recorded at $\tau = 5, 55, \text{ and } 195$ s. From the fluorescence intensity, we can infer ρ_0 and c_0 at different locations in the channel through a calibration curve using known concentrations s . The concentration gradient is quantified by measuring the intensity profile across the channel width, which shows that the concentration field evolves from a steep box-shaped distribution at early times to a progressively more flat distribution at later times; see Fig. 4. Since the measurement plane is placed at $z = 0$, away from the compressed streaming rolls near the top and bottom boundaries, the evolution of the concentration field is governed purely by diffusion free from advection at early times. With this assumption, the diffusivity D of each solution can be extracted from the concentration profile s at early times by a simple numerical model of molecular diffusion in one dimension (1D) in the transverse y direction with zero-flux boundary conditions at the walls $y = \pm \frac{1}{2}W$. It should be noted that the diffusivity D is measured in the presence of the ultrasound field, which might be different from the situation without ultrasound owing to the barodiffusion [55] and the possible interaction between the Ficoll molecules and sound waves. The fitted, estimated expression for D as a function of the solute concentration s is listed in Table II.

B. Streaming in inhomogeneous solutions

With the nine different solutions S1–S9 of Table I and the general theory summarized in Sec. II, we are now in a position for a detailed study of the acoustic streaming in inhomogeneous solutions. We quantify the magnitude of a given inhomogeneity by the excess mass density $\hat{\rho}_*$ and the excess speed of sound \hat{c}_* , based on local values in the center and in the side of the channel [see Fig. 3(b)]:

$$\hat{\rho}_* = \frac{\rho_{\text{cntr}}}{\rho_{\text{side}}} - 1, \quad \hat{c}_* = \frac{c_{\text{cntr}}}{c_{\text{side}}} - 1. \quad (9)$$

We begin by studying solutions S1–S4 that, as can be seen from Table I, are chosen for their specific dependencies

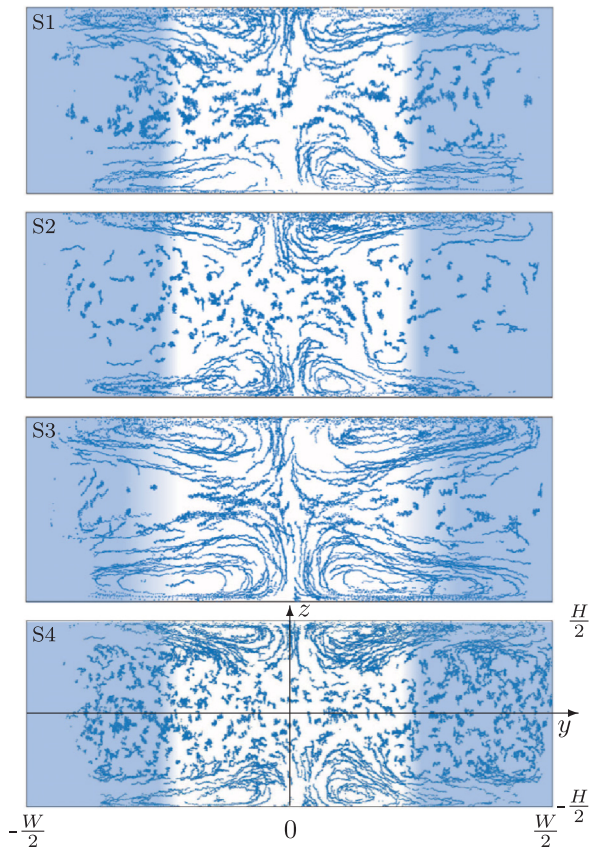


FIG. 5. The particle positions (blue points) in the vertical y - z cross section of width $W = 375 \mu\text{m}$ and height $H = 133 \mu\text{m}$ overlaid from 100 frames between $\tau = 20$ and 30 s for the inhomogeneous solutions S1, S2, S3, and S4 listed in Table I. The color plot represents the concentration of the solute molecules from low (dark) to high (white).

on $\hat{\rho}_*$ and \hat{c}_* : S1 depends only on $\hat{\rho}_*$, S2 only on \hat{c}_* , S3 on both with opposite sign, and S4 on both with the same sign. Moreover, in all four cases, the center liquid is chosen so as to be stabilized by the acoustic body force acting on the inhomogeneous fluid, which avoids undesirable particle motion due to the relocation of the two liquids [50]. The overlaid particle positions from $\tau = 20$ to 30 s in different gradients for S1–S4 are shown in Fig. 5. It is seen that streaming is suppressed in the bulk for all four solutions and is only manifested by flat streaming rolls located near the top and bottom walls at $z = \pm \frac{1}{2}H$, in full agreement with our previous findings for an iodixanol solution with only density dependency and no sound speed dependency [53]. All streaming patterns are similar, exhibiting four vortices with no apparent symmetry around the vortex centers and having a larger width close to the center $y = 0$ than to the side walls at $y = \pm \frac{1}{2}W$.

The asymmetry in the streaming rolls can be explained by the evolution of the concentration field $s(\mathbf{r}, \tau)$ near the top and the bottom walls at early times. Initially by

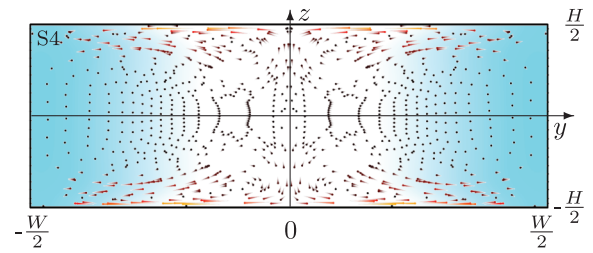


FIG. 6. Numerical simulation (see Sec. II E) in the vertical y - z cross section for solution S4 (10% Ficoll PM400 and Milli-Q) of Table I with the parameters given in Table II in a standing half-wave pressure field of energy density $E_{ac} = 52$ Pa corresponding to S4 in Fig. 5. The comet-tail plot shows the position (dots) and velocity (colored comet tails) of 1000 polystyrene 500-nm-diameter tracer particles at $\tau = 25$ s that started out in a regular 50×20 mesh at $\tau = 0$ s. The color plot represents the concentration of the solute molecules from $s \approx 0.015$ (blue) to $s \approx 0.085$ (white).

construction, s exhibits a steep, nearly vertical boxlike distribution; the acoustic body force \mathbf{f}_{ac} stabilizes the fluid in the center stream and prevents advective recirculation in the bulk [52]. However, near the top and bottom walls, the compressed streaming flow transports the center solution toward the sides, causing wedges with nearly 45° slopes to form in the concentration field s at regions near $y = 0$ and $z = \pm \frac{1}{2}H$. Because \mathbf{f}_{ac} is parallel to the concentration gradient, the wedges lead to a weaker \mathbf{f}_{ac} in the horizontal direction and, therefore, the streaming rolls have larger curvature near the center of the channel. These wedges are difficult to resolve experimentally, so to confirm the above hypothesis, we perform a numerical simulation of the evolution of the concentration field and the streaming field using COMSOL Multiphysics as described in Sec. II E. In Fig. 6, we show the results of such a simulation for solution S4 at time $\tau = 25$ s after injection into the device having a transverse standing half-wave present as in the experiment. The wedge shape in the concentration field is clearly seen in the transition from high (white) to low (blue) concentration near the top center and bottom center of the cross section. Moreover, the simulated particle motion shows the observed asymmetric vortices being broader near the center $y \approx 0$ than compared to the sides at $y \approx \pm \frac{1}{2}W$. In the Supplemental Material [58], we have placed movies showing the time evolution for $0 < \tau < 40$ s, of which Fig. 6 is the single frame at $\tau = 25$ s.

C. Time evolution of the streaming suppression

To follow the time evolution and final breakdown of the streaming suppression, the tracer particle motion is tracked for 200 s after stopping the flow. The streaming evolution is shown in Fig. 7 for the inhomogeneous Ficoll-water solution S7 of Table I. At early times, $\tau = 35$ s in Fig. 7, the streaming is greatly suppressed in the bulk, and

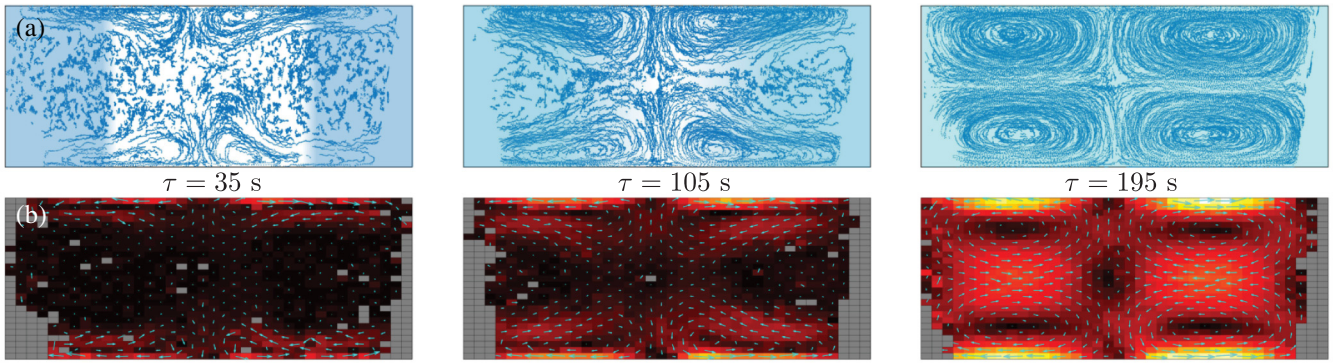


FIG. 7. The acoustic streaming observed in the vertical y - z cross section of width $W = 375 \mu\text{m}$ and height $H = 133 \mu\text{m}$ at time $\tau = 5, 35$, and 195 s using the 10% Ficoll PM70 solution S7 of Table I. (a) Experimental particle positions (blue points) with a color plot of the solute concentration as in Fig. 5. (b) Color plot of the streaming velocity amplitude $|\langle v_2 \rangle|$ from $0 \mu\text{m/s}$ (black) to $45 \mu\text{m/s}$ (white) overlaid with a vector plot (cyan) of $\langle v_2 \rangle$. Spatial bins with no data points are excluded (gray).

the four streaming rolls are confined to the walls with an asymmetric pattern. As time evolves, $\tau = 105 \text{ s}$ in Fig. 7, the streaming rolls grow toward homogeneous steady-state Rayleigh streaming, but the asymmetric pattern is still apparent. At later times, $\tau = 195 \text{ s}$ in Fig. 7, the streaming pattern is identical to that of a homogeneous system as diffusion and advection have homogenized the system.

To quantify the suppression of streaming, we use the streaming vortex size Δ that we introduced in Ref. [53], defined as the distance between the center of the flow roll, situated at $y = \pm \frac{1}{4}W$ where streaming velocity is zero, and the nearest wall. In all homogeneous states, we find $\Delta_{\text{hom}} = (27.4 \pm 2.1) \mu\text{m}$ close to $(\frac{1}{2} - \frac{1}{\sqrt{12}})H = 28.1 \mu\text{m}$ found from $\langle v_{2y} \rangle = 0$ in Eq. (7a). We then study the time evolution of the six inhomogeneous solutions S4–S9 of Table I, all created by injecting a given Ficoll solution into the center inlet and Milli-Q water into the side inlets. The time evolution of the streaming flow is characterized by the normalized vortex size $\Delta/\Delta_{\text{hom}}$, as shown in Fig. 8(a) for Ficoll PM70. We see that $\Delta/\Delta_{\text{hom}}$ increases slowly at early times and then undergoes a transition to a faster increase. The transition occurs at different times for different Ficoll concentrations. This result indicates that the evolution of the concentration field is dominated by diffusion at early times, whereas the advection due to the streaming plays a minor role. When reaching a critically weak inhomogeneity, the streaming rolls have grown sufficiently so that advection starts to play a more important role. A transition occurs, after which the rate of change of $\Delta/\Delta_{\text{hom}}$ is increased, since the inhomogeneity now is weakened by both diffusion and advection. This transition occurs at earlier times if the initial concentration of Ficoll is lower for two reasons: the diffusivity is larger (see Table II) and the initial solution gradients are weaker, resulting in a smaller \mathbf{f}_{ac} . Hence, at a given time τ , the transition occurs earlier and the rate of change of $\Delta/\Delta_{\text{hom}}$ is larger for a lower initial Ficoll concentration compared to

a higher one. For all concentrations, the streaming rolls expand from the walls into the bulk as the inhomogeneity is smeared out and, finally, they become the same as for homogeneous streaming, indicated by $\Delta/\Delta_{\text{hom}} \approx 1$ at late times in Fig. 8(a).

The time evolution also depends on the mass of the molecules that cause the inhomogeneity, which affects the diffusivity. In Fig. 8(b) is shown the streaming roll evolution for Ficoll PM400, which has 5.7 times larger mass and 25% lower diffusivity (at $s = 0.1$) compared to Ficoll PM70 in Fig. 8(a). The rate of change of $\Delta/\Delta_{\text{hom}}$ is lower and the transition point between diffusion- and advection-diffusion-dominated regimes is shifted to later times for all initial concentrations. Before the transition

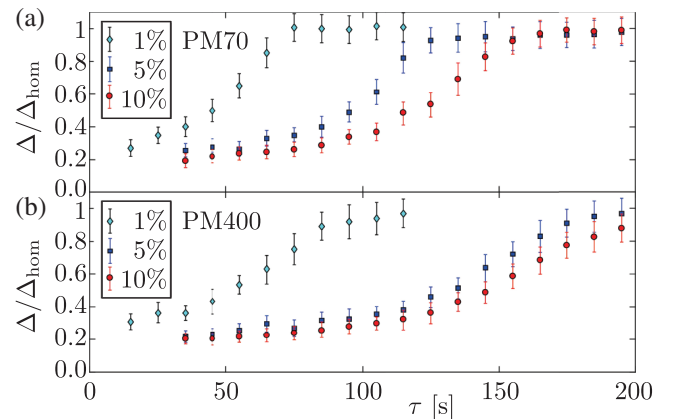


FIG. 8. The normalized vortex size $\Delta/\Delta_{\text{hom}}$ versus time τ using (a) Ficoll PM70 solution S7–S9 and (b) Ficoll PM400 solution S4–S6 with 1%, 5%, or 10% mass concentration in the center inlet and Milli-Q water in the side inlets. $\Delta(\tau)$ is calculated from overlaid 100 frames recorded in intervals of 0.1 s from $\tau - 5 \text{ s}$ to $\tau + 5 \text{ s}$, so each data point represents a time interval of 10 s . Each error bar is the error computed when fitting the raw data by a quadratic function in z to determine the center of the streaming vortex.

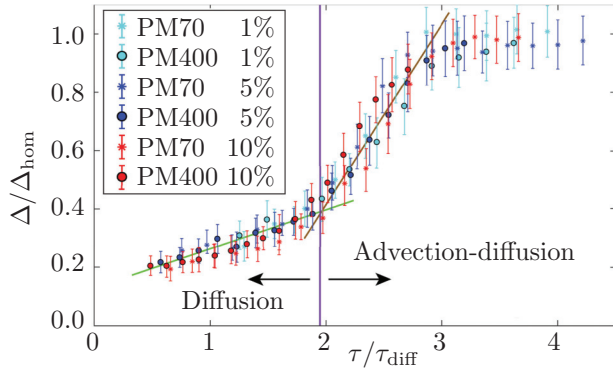


FIG. 9. Plot of the normalized vortex size $\Delta/\Delta_{\text{hom}}$ versus rescaled time τ/τ_{diff} , where $\tau_{\text{diff}} = (\frac{1}{4}W)^2/(2D)$ is the diffusion time for the given solute molecule, for Ficoll solutions S4–S9 from Fig. 8. The green line indicates the early time diffusion-dominated dynamics, while the brown line indicates the late time advection-diffusion-dominated dynamics. The two 1% solutions have been shifted by $0.9 \tau_{\text{diff}}$; see the text.

occurs, the particles in the bulk only experience acoustic radiation force without the competition with the streaming-induced Stokes drag force. In addition, the duration of the diffusion-dominated regime can be controlled by selecting appropriate gradients, providing sufficient time to move small particles by acoustic radiation force. This feature in an inhomogeneous medium breaks the small-size barrier in acoustophoresis, which enables the manipulation of submicrometer particles.

To further validate that the evolution of Δ is dominated by diffusion at early times, we plot in Fig. 9 $\Delta/\Delta_{\text{hom}}$ versus the rescaled time τ/τ_{diff} , where $\tau_{\text{diff}} = (\frac{1}{4}W)^2/(2D)$ is the diffusion time for the given solute. By this rescaling, the difference in diffusivity between the solutions is removed and a nearly perfect collapse of the six data sets is observed for $\tau \lesssim 2\tau_{\text{diff}}$. For $\tau \approx 2\tau_{\text{diff}}$, the previously described transition to the advection-diffusion regime occurs and, for $\tau \gtrsim 2\tau_{\text{diff}}$, the collapse is not as good, as the advection part does not scale with the diffusion time. In Fig. 9, we see a higher rate of change and a larger spread in the data points after the transition. As \mathbf{f}_{ac} is weak in the two 1% solutions, advection plays a role from the beginning. Time zero is therefore ill defined and, consequently, we have shifted these two data sets by $0.9 \tau_{\text{diff}}$ in time to make the transition point coincide with that of the four 5% and 10% solutions.

In a final analysis, we tie the evolution of the normalized vortex size $\Delta/\Delta_{\text{hom}}$ directly with the underlying concentration difference between the center and the sides of the sample. By a first-order Taylor expansion of the inhomogeneous density $\rho_0(s)$ and sound speed $c_0(s)$, we define the normalized concentration difference \hat{s}_* as

$$\hat{s}_* = \hat{\rho}_* \frac{\rho_0(0)}{\frac{d}{ds}\rho_0(0)} = \hat{c}_* \frac{c_0(0)}{\frac{d}{ds}c_0(0)}. \quad (10)$$

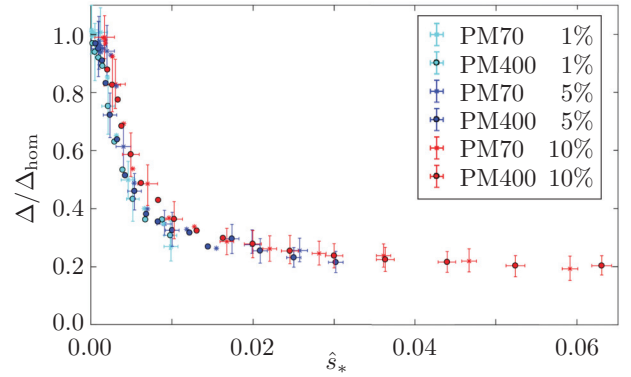


FIG. 10. The normalized vortex size $\Delta/\Delta_{\text{hom}}$ plotted versus the normalized concentration difference \hat{s}_* for the six different Ficoll solutions S4–S9. For clarity, the error bars are only shown for every third data point for $\hat{s}_* < 0.02$.

In Fig. 10, we plot $\Delta/\Delta_{\text{hom}}$ for all six Ficoll-Milli-Q solutions S4–S9 of I as a function of \hat{s}_* and thus only implicitly as a function of time τ . We observe that all six data sets fall on a single curve that increases as s decreases, giving strong support to the hypothesis that the suppression of the acoustic streaming in the bulk is governed by \mathbf{f}_{ac} resulting from the concentration profile s . We see that streaming is efficiently suppressed for $\hat{s}_* > 0.01$, where the flow roll size Δ is less than 30% of the homogeneous size Δ_{hom} .

V. CONCLUSION

The efficient suppression of acoustic streaming in inhomogeneous media presents opportunities for in-line, label-free filters to align or separate submicrometer particles by acoustic radiation forces. In this paper, we investigate experimentally acoustic streaming, in a half-wavelength resonator, for aqueous solutions that are made spatially inhomogeneous in density and compressibility by a solute concentration gradient. The results show that acoustic streaming patterns are very sensitive to such inhomogeneities. Acoustic streaming in the bulk of inhomogeneous fluids is suppressed by confinement of the recirculating streaming rolls near the boundaries parallel to the direction of sound propagation. As corroborated by numerical simulations, this suppression is caused by an inhomogeneity-induced acoustic body force \mathbf{f}_{ac} . The suppressed streaming rolls exhibit an asymmetry pattern due to a local streaming-induced deformation of the molecular concentration field near the walls where streaming is generated. The streaming rolls grow over time primarily due to diffusion, but for late times, advection plays an important role as \mathbf{f}_{ac} vanishes and the system becomes homogeneous. For Ficoll solutions, \mathbf{f}_{ac} decays steadily over a time span of 70 to 200 s and $\Delta < 0.3\Delta_{\text{hom}}$ is detected for inhomogeneities in the Ficoll mass fraction above as little as 1%.

Our findings indicate that streaming-free particle separation can be carried out in the bulk of the acoustic resonator during several seconds by adding just 1% mass fraction of Ficoll molecules to the central inlet fluid stream. We see a clear potential for this type of acoustic streaming suppression to enable acoustic manipulation, enrichment, and fractionation of particles in the submicrometer range by acoustophoresis.

ACKNOWLEDGMENTS

W.Q. was supported by the People Programme (Marie Curie Actions) EC-FP7/2007-2013, REA Grant No. 609405 (COFUNDPostdocDTU). P.A. was supported by Grant No. 2016-04836 from the Swedish Research Council, Grant No. ICA16-0002 from the Swedish Foundation for Strategic Research, and Grant No. 20180837 from the Crafoord Foundation. The authors are grateful to R. Barnkob and M. Rossi, Universität der Bundeswehr München, for providing the software GDPTlab [59,60], and Jeppe Revall Frisvad, Technical University of Denmark, for accessing the refractometer.

-
- [1] P. Augustsson, J. T. Karlsen, H.-W. Su, H. Bruus, and J. Voldman, Iso-acoustic focusing of cells for size-insensitive acousto-mechanical phenotyping, *Nat. Commun.* **7**, 11556 (2016).
 - [2] E. M. Darling, and D. Di Carlo, High-throughput assessment of cellular mechanical properties, *Annu. Rev. Biomed. Eng.* **17**, 35 (2015).
 - [3] W. H. Grover, A. K. Bryan, M. Diez-Silva, S. Suresh, J. M. Higgins, and S. R. Manalis, Measuring single-cell density, *Proc. Natl. Acad. Sci. USA* **108**, 10992 (2011).
 - [4] O. Otto, P. Rosendahl, A. Mietke, S. Golfier, C. Herold, D. Klaue, S. Girardo, S. Pagliara, A. Ekpenyong, A. Jacobi, M. Wobus, N. Topfner, U. F. Keyser, J. Mansfeld, E. Fischer-Friedrich, and J. Guck, Real-time deformability cytometry: On-the-fly cell mechanical phenotyping, *Nat. Meth.* **12**, 199 (2015).
 - [5] J. A. Davis, D. W. Inglis, K. J. Morton, D. A. Lawrence, L. R. Huang, S. Y. Chou, J. C. Sturm, and R. H. Austin, Deterministic hydrodynamics: Taking blood apart, *Proc. Natl. Acad. Sci. USA* **103**, 14779 (2006).
 - [6] F. Petersson, L. Åberg, A. M. Swärd-Nilsson, and T. Laurell, Free flow acoustophoresis: Microfluidic-based mode of particle and cell separation, *Anal. Chem.* **79**, 5117 (2007).
 - [7] M. Dhar, J. N. Lam, T. Walser, S. M. Dubinett, M. B. Rettig, and D. Di Carlo, Functional profiling of circulating tumor cells with an integrated vortex capture and single-cell protease activity assay, *Proc. Natl. Acad. Sci. USA* **115**, 9986 (2018).
 - [8] E. Ozkumur *et al.*, Inertial focusing for tumor antigen-dependent and -independent sorting of rare circulating tumor cells, *Sci. Transl. Med.* **5**, 179ra47 (2013).
 - [9] C. Magnusson, P. Augustsson, A. Lenshof, Y. Ceder, T. Laurell, and H. Lilja, Clinical-scale cell-surface-marker independent acoustic microfluidic enrichment of tumor cells from blood, *Anal. Chem.* **89**, 11954 (2017).
 - [10] A. M. Foudeh, T. F. Didar, T. Veres, and M. Tabrizian, Microfluidic designs and techniques using lab-on-a-chip devices for pathogen detection for point-of-care diagnostics, *Lab Chip* **12**, 3249 (2012).
 - [11] R. T. Davies, J. Kim, S. C. Jang, E. J. Choi, Y. S. Gho, and J. Park, Microfluidic filtration system to isolate extracellular vesicles from blood, *Lab Chip* **12**, 5202 (2012).
 - [12] P. Li, M. Kaslan, S. H. Lee, J. Yao, and Z. Q. Gao, Progress in exosome isolation techniques, *Theranostics* **7**, 789 (2017).
 - [13] K. Lee, H. Shao, R. Weissleder, and H. Lee, Acoustic purification of extracellular microvesicles, *ACS Nano* **9**, 2321 (2015).
 - [14] P. Ohlsson, K. Petersson, P. Augustsson, and T. Laurell, Acoustic impedance matched buffers enable separation of bacteria from blood cells at high cell concentrations, *Sci. Rep.* **8**, 9156 (2018).
 - [15] A. Ku, H. C. Lim, M. Evander, H. Lilja, T. Laurell, S. Scheduling, and Y. Ceder, Acoustic enrichment of extracellular vesicles from biological fluids, *Anal. Chem.* **90**, 8011 (2018).
 - [16] W. L. Nyborg, Acoustic streaming due to attenuated plane waves, *J. Acoust. Soc. Am.* **25**, 68 (1953).
 - [17] W. L. Nyborg, Acoustic streaming near a boundary, *J. Acoust. Soc. Am.* **30**, 329 (1958).
 - [18] J. Lighthill, Acoustic streaming, *J. Sound Vibr* **61**, 391 (1978).
 - [19] N. Riley, Steady streaming, *Annu. Rev. Fluid Mech.* **33**, 43 (2001).
 - [20] P. B. Muller, and H. Bruus, Theoretical study of time-dependent, ultrasound-induced acoustic streaming in microchannels, *Phys. Rev. E* **92**, 063018 (2015).
 - [21] H. Bailliet, V. Gusev, R. Raspet, and R. A. Hiller, Acoustic streaming in closed thermoacoustic devices, *J. Acoust. Soc. Am.* **110**, 1808 (2001).
 - [22] M. Hamilton, Y. Ilinskii, and E. Zabolotskaya, Thermal effects on acoustic streaming in standing waves, *J. Acoust. Soc. Am.* **114**, 3092 (2003).
 - [23] P. Marmottant, and S. Hilgenfeldt, Controlled vesicle deformation and lysis by single oscillating bubbles, *Nature* **423**, 153 (2003).
 - [24] L. van der Sluis, M. Versluis, M. Wu, and P. Wesselink, Passive ultrasonic irrigation of the root canal: A review of the literature, *Int. Endod. J.* **40**, 415 (2007).
 - [25] J. Wu, and W. L. Nyborg, Ultrasound, cavitation bubbles and their interaction with cells, *Adv. Drug Delivery Rev.* **60**, 1103 (2008).
 - [26] A. A. Doinikov, and A. Bouakaz, Theoretical investigation of shear stress generated by a contrast microbubble on the cell membrane as a mechanism for sonoporation, *J. Acoust. Soc. Am.* **128**, 11 (2010).
 - [27] E. Trinh, and J. Robey, Experimental study of streaming flows associated with ultrasonic levitators, *Phys. Fluids* **6**, 3567 (1994).
 - [28] A. Yarin, G. Brenn, O. Kastner, D. Rensink, and C. Tropea, Evaporation of acoustically levitated droplets, *J. Fluid Mech.* **399**, 151 (1999).
 - [29] C. Eckart, Vortices and streams caused by sound waves, *Phys. Rev.* **73**, 68 (1948).

- [30] Lord Rayleigh, On the circulation of air observed in Kundt's tubes, and on some allied acoustical problems, *Philos. Trans. R. Soc. London* **175**, 1 (1884).
- [31] H. Schlichting, Berechnung ebener periodischer grenzschichtströmungen, *Phys. Z.* **33**, 327 (1932).
- [32] M. Hamilton, Y. Ilinskii, and E. Zabolotskaya, Acoustic streaming generated by standing waves in two-dimensional channels of arbitrary width, *J. Acoust. Soc. Am.* **113**, 153 (2003).
- [33] P. B. Muller, M. Rossi, A. G. Marin, R. Barnkob, P. Augustsson, T. Laurell, C. J. Kähler, and H. Bruus, Ultrasound-induced acoustophoretic motion of microparticles in three dimensions, *Phys. Rev. E* **88**, 023006 (2013).
- [34] S. A. Elder, Cavitation microstreaming, *J. Acoust. Soc. Am.* **31**, 54 (1959).
- [35] C. P. Lee, and T. G. Wang, Outer acoustic streaming, *J. Acoust. Soc. Am.* **88**, 2367 (1990).
- [36] P. Tho, R. Manasseh, and A. Ooi, Cavitation microstreaming patterns in single and multiple bubble systems, *J. Fluid Mech.* **576**, 191 (2007).
- [37] H. Bruus, J. Dual, J. Hawkes, M. Hill, T. Laurell, J. Nilsson, S. Radel, S. Sadhal, and M. Wiklund, Forthcoming lab on a chip tutorial series on acoustofluidics: Acoustofluidics-exploiting ultrasonic standing wave forces and acoustic streaming in microfluidic systems for cell and particle manipulation, *Lab Chip* **11**, 3579 (2011).
- [38] R. Barnkob, P. Augustsson, T. Laurell, and H. Bruus, Acoustic radiation- and streaming-induced microparticle velocities determined by microparticle image velocimetry in an ultrasound symmetry plane, *Phys. Rev. E* **86**, 056307 (2012).
- [39] B. Hammarström, T. Laurell, and J. Nilsson, Seed particle enabled acoustic trapping of bacteria and nanoparticles in continuous flow systems, *Lab Chip* **12**, 4296 (2012).
- [40] D. J. Collins, B. Morahan, J. Garcia-Bustos, C. Doerig, M. Plebanski, and A. Neild, Two-dimensional single-cell patterning with one cell per well driven by surface acoustic waves, *Nat. Commun.* **6**, 8686 (2015).
- [41] A. Marin, M. Rossi, B. Rallabandi, C. Wang, S. Hilgenfeldt, and C. J. Kähler, Three-dimensional Phenomena in Microbubble Acoustic Streaming, *Phys. Rev. Appl.* **3**, 041001 (2015).
- [42] P. Hahn, I. Leibacher, T. Baasch, and J. Dual, Numerical simulation of acoustofluidic manipulation by radiation forces and acoustic streaming for complex particles, *Lab Chip* **15**, 4302 (2015).
- [43] F. Guo, Z. Mao, Y. Chen, Z. Xie, J. P. Lata, P. Li, L. Ren, J. Liu, J. Yang, M. Dao, S. Suresh, and T. J. Huang, Three-dimensional manipulation of single cells using surface acoustic waves, *Proc. Natl. Acad. Sci. USA* **113**, 1522 (2016).
- [44] M. Antfolk, P. B. Muller, P. Augustsson, H. Bruus, and T. Laurell, Focusing of sub-micrometer particles and bacteria enabled by two-dimensional acoustophoresis, *Lab Chip* **14**, 2791 (2014).
- [45] Z. Mao, P. Li, M. Wu, H. Bachman, N. Mesyngier, X. Guo, S. Liu, F. Costanzo, and T. J. Huang, Enriching nanoparticles via acoustofluidics, *ACS Nano* **11**, 603 (2017).
- [46] D. Carugo, T. Octon, W. Messaoudi, A. L. Fisher, M. Carboni, N. R. Harris, M. Hill, and P. Glynn-Jones, A thin-reflector microfluidic resonator for continuous-flow concentration of microorganisms: A new approach to water quality analysis using acoustofluidics, *Lab Chip* **14**, 3830 (2014).
- [47] D. J. Collins, Z. Ma, J. Han, and Y. Ai, Continuous microvortex-based nanoparticle manipulation via focused surface acoustic waves, *Lab Chip* **17**, 91 (2017).
- [48] M. Wu, Z. Mao, K. Chen, H. Bachman, Y. Chen, J. Rufo, L. Ren, P. Li, L. Wang, and T. J. Huang, Acoustic separation of nanoparticles in continuous flow, *Adv. Funct. Mater.* **27**, 1606039 (2017).
- [49] P. Sehgal, and B. J. Kirby, Separation of 300 and 100 nm particles in fabry-perot acoustofluidic resonators, *Anal. Chem.* **89**, 12192 (2017).
- [50] S. Deshmukh, Z. Brzozka, T. Laurell, and P. Augustsson, Acoustic radiation forces at liquid interfaces impact the performance of acoustophoresis, *Lab Chip* **14**, 3394 (2014).
- [51] J. T. Karlsen, P. Augustsson, and H. Bruus, Acoustic Force Density Acting on Inhomogeneous Fluids in Acoustic Fields, *Phys. Rev. Lett.* **117**, 114504 (2016).
- [52] J. T. Karlsen, and H. Bruus, Acoustic Tweezing and Patterning of Concentration Fields in Microfluidics, *Phys. Rev. Appl.* **7**, 034017 (2017).
- [53] J. T. Karlsen, W. Qiu, P. Augustsson, and H. Bruus, Acoustic Streaming and its Suppression in Inhomogeneous Fluids, *Phys. Rev. Lett.* **120**, 054501 (2018).
- [54] J. P. Koulakis, S. Pree, A. L. F. Thornton, and S. Putterman, Trapping of plasma enabled by pycnoclinic acoustic force, *Phys. Rev. E* **98**, 043103 (2018).
- [55] L. D. Landau, and E. M. Lifshitz, *Fluid Mechanics* (Pergamon Press, Oxford, 1993). 2nd ed., 6.
- [56] COMSOL Multiphysics 5.2, www.comsol.com (2015).
- [57] To fix E_{ac} , which varies due to small shifts in resonance frequency as $s(\mathbf{r}, \tau)$ evolves, we compensate by adjusting the sidewall actuation amplitude $d_0(\tau)$ iteratively; see also Ref. [63].
- [58] See Supplemental Material at <http://link.aps.org/supplemental/10.1103/PhysRevApplied.11.024018> for details on the fitting leading to $\rho_0(s)$, $c_0(s)$, $\eta_0(s)$, and $D(s)$, as well as for COMSOL simulations of the time evolution of the concentration field s and the trajectories of 500-nm-diameter and 1000-nm-diameter tracer particles in solution S4.
- [59] R. Barnkob, C. J. Kähler, and M. Rossi, General defocusing particle tracking, *Lab Chip* **15**, 3556 (2015).
- [60] GDTPlab – how to get it, Institut für Strömungsmechanik und Aerodynamik, Universität der Bundeswehr, Werner Heisenberg Weg 39, 85577 Neubiberg, Germany, https://www.unibw.de/lrt7/gdpt-1/gdptlab-how_to_get_it, accessed 26 September 2018.
- [61] O. Manneberg, B. Vanherberghen, B. Önfelt, and M. Wiklund, Flow-free transport of cells in microchannels by frequency-modulated ultrasound, *Lab Chip* **9**, 833 (2009).
- [62] R. Barnkob, P. Augustsson, T. Laurell, and H. Bruus, Measuring the local pressure amplitude in microchannel acoustophoresis, *Lab Chip* **10**, 563 (2010).
- [63] P. B. Muller, R. Barnkob, M. J. H. Jensen, and H. Bruus, A numerical study of microparticle acoustophoresis driven by acoustic radiation forces and streaming-induced drag forces, *Lab Chip* **12**, 4617 (2012).